

University of Groningen

## Toward Understanding Space-Charge Limited Current Measurements on Metal Halide Perovskites

Duijnste, Elisabeth A.; Ball, James M.; Le Corre, Vincent M.; Koster, L. Jan Anton; Snaith, Henry J.; Lim, Jongchul

*Published in:*  
 ACS Energy Letters

*DOI:*  
[10.1021/acsenergylett.9b02720](https://doi.org/10.1021/acsenergylett.9b02720)

**IMPORTANT NOTE: You are advised to consult the publisher's version (publisher's PDF) if you wish to cite from it. Please check the document version below.**

*Document Version*  
 Publisher's PDF, also known as Version of record

*Publication date:*  
 2020

[Link to publication in University of Groningen/UMCG research database](#)

*Citation for published version (APA):*

Duijnste, E. A., Ball, J. M., Le Corre, V. M., Koster, L. J. A., Snaith, H. J., & Lim, J. (2020). Toward Understanding Space-Charge Limited Current Measurements on Metal Halide Perovskites. *ACS Energy Letters*, 5(2), 376-384. <https://doi.org/10.1021/acsenergylett.9b02720>

### Copyright

Other than for strictly personal use, it is not permitted to download or to forward/distribute the text or part of it without the consent of the author(s) and/or copyright holder(s), unless the work is under an open content license (like Creative Commons).

The publication may also be distributed here under the terms of Article 25fa of the Dutch Copyright Act, indicated by the "Taverne" license. More information can be found on the University of Groningen website: <https://www.rug.nl/library/open-access/self-archiving-pure/taverne-amendment>.

### Take-down policy

If you believe that this document breaches copyright please contact us providing details, and we will remove access to the work immediately and investigate your claim.

*Downloaded from the University of Groningen/UMCG research database (Pure): <http://www.rug.nl/research/portal>. For technical reasons the number of authors shown on this cover page is limited to 10 maximum.*

# Toward Understanding Space-Charge Limited Current Measurements on Metal Halide Perovskites

Elisabeth A. Duijnste, James M. Ball, Vincent M. Le Corre, L. Jan Anton Koster,\* Henry J. Snaith,\* and Jongchul Lim\*



Cite This: *ACS Energy Lett.* 2020, 5, 376–384



Read Online

ACCESS |



Metrics & More

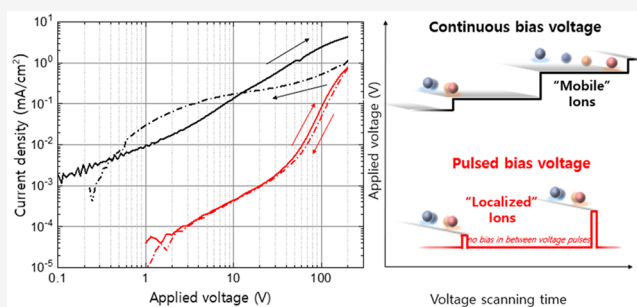


Article Recommendations



Supporting Information

**ABSTRACT:** Metal halide perovskite semiconductors have sprung to the forefront of research into optoelectronic devices and materials, largely because of their remarkable photovoltaic efficiency records above 25% in single-junction devices and 28% in tandem solar cells, achieved within a decade of research. Despite this rapid progress, ionic conduction within the semiconductor still puzzles the community and can have a significant impact on all metal halide perovskite-based optoelectronic devices because of its influence upon electronic and optoelectronic processes. This phenomenon thus also makes the interpretation of electrical characterization techniques, which probe the fundamental properties of these materials, delicate and complex. For example, space-charge limited current measurements are widely used to probe defect densities and carrier mobilities in perovskites. However, the influence of mobile ions upon these measurements is significant but has yet to be considered. Here we report the effect of mobile ions upon electronic conductivity during space-charge limited current measurements of MAPbBr<sub>3</sub> single crystals and show that conventional interpretations deliver erroneous results. We introduce a pulsed-voltage space-charge limited current procedure to achieve reproducible current–voltage characteristics without hysteresis. From this revised pulsed current–voltage sweep, we elucidate a lower bound trap-density value of  $2.8 \pm 1.8 \times 10^{12} \text{ cm}^{-3}$  in MAPbBr<sub>3</sub> single crystals. This work will lead to more accurate characterization of halide perovskite semiconductors and ultimately more effective device optimization.



The dawn of a new era in optoelectronic research has emerged with the recent studies on organic–inorganic metal halide perovskites.<sup>1–3</sup> Their long carrier lifetimes, sufficient charge carrier mobility, ensuing long-range charge transport,<sup>4</sup> low levels of electronic disorder, and low-cost device production render perovskites as one of the most exceptional and competitive optoelectronic materials for many applications such as photovoltaic devices,<sup>1,5</sup> field-effect transistors,<sup>6</sup> light-emitting diodes,<sup>7</sup> photo and radiation detectors,<sup>8</sup> and lasers.<sup>9,10</sup>

The accurate characterization of a semiconductor's fundamental properties is important for the development of electronic and optoelectronic devices. Among the various charge transport characterization techniques available,<sup>11</sup> the space-charge limited current (SCLC) measurement is one of the most commonly used steady-state techniques. By measuring current-density–voltage ( $J$ – $V$ ) characteristics, the electron- and hole-transport and injection properties can be studied, without light illumination for the generation of charge carriers. During this measurement, the injection of current is

used as a powerful probe for the study of both the defect states in the bandgap of semiconductors and the charge carrier mobility.<sup>12–15</sup> Conventionally, for the case of unipolar conduction, the  $J$ – $V$  curve first follows Ohm's law (1.  $J \propto V$  in Figure 1a), where the conductivity is determined by the background charge carriers.<sup>15,16</sup> When the injected free carrier concentration exceeds this background charge carrier concentration, the space-charge effect is said to occur, where the current is limited by the buildup of space-charge (2.  $J \propto V^2$  in Figure 1a), and the current-density follows the Mott–Gurney law:<sup>17</sup>

$$J_{\text{SCLC}} = \frac{9}{8} \epsilon_0 \epsilon_r \mu \frac{V^2}{L^3} \quad (1)$$

Received: December 13, 2019

Accepted: January 3, 2020

Published: January 3, 2020



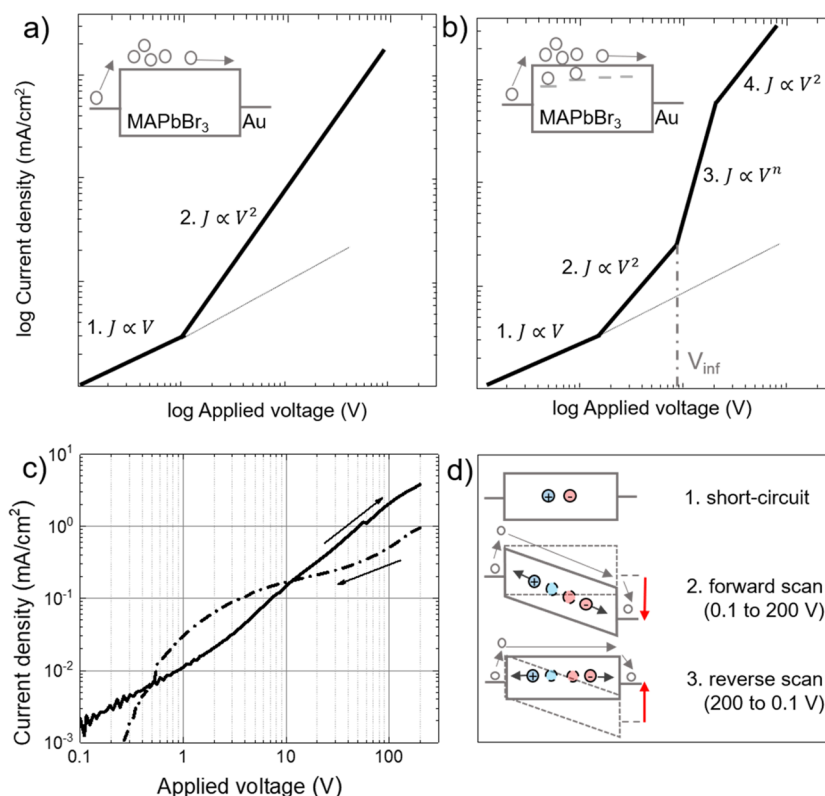


**Figure 1.** Schematic illustration of the principle and hysteresis in SCLC measurement. (a) SCLC behavior for a trap-free semiconductor. Two charge transport regions are visible: (1.  $J \propto V$ ) Ohmic region and (2.  $J \propto V^2$ ) SCLC region. (b) SCLC behavior for a semiconductor with trap states. Four charge transport regions are visible: (1.  $J \propto V$ ) Ohmic region, (2.  $J \propto V^2$ ) trap SCLC region, (3.  $J \propto V^n$ ,  $n > 2$ ) trap-filled limited region, and (4.  $J \propto V^2$ ) SCLC region in the absence of trapping. Panels a and b show example schematics of  $J$ - $V$  curves, and their scales are dependent on the sample characteristics and dimensions. (c) Large hysteresis between forward (solid line) and reverse (dashed line)  $J$ - $V$  traces during the SCLC measurement. (d) Schematic illustration of ion movement during the SCLC measurement. At short circuit (1) mobile ions are distributed across the crystal. Upon application of a positive voltage during the forward scan (2), mobile ions drift toward the electrode interfaces. Mobile ions are still displaced toward the electrode interfaces during the reverse scan (3).

where  $V$  is the applied voltage,  $L$  the thickness of the active material,  $\epsilon_r$  the dielectric constant (25.5 for methylammonium lead tribromide (MAPbBr<sub>3</sub>) in this study),<sup>18</sup>  $\epsilon_0$  the permittivity of free space, and  $\mu$  the mobility. However, in real materials and devices, the presence of electronic trap states with energy levels within the bandgap can significantly change the actual shape and magnitude of the  $J$ - $V$  characteristics.<sup>19</sup> In Figure 1b, we show the theoretically predicted  $J$ - $V$  trace for a semiconductor with a distribution of traps which are initially empty. Now, with the presence of traps, only a fraction of the injected carriers is free, and consequently  $\mu$  is replaced by an effective mobility,  $\mu_{\text{eff}} = \mu \cdot \theta$ , where  $\theta$  is the free-carrier fraction (with respect to trapped charge) and is determined by the number and depth of the traps.<sup>12,20</sup> We define the voltage required to support the total trapped space-charge as the onset voltage ( $V_{\text{ons}}$ ).  $V_{\text{ons}}$  is often used to calculate the defect density by using the following equation:<sup>15</sup>

$$V_{\text{ons}} \approx \frac{en_t L^2}{2\epsilon_0 \epsilon_r} \quad (2)$$

where  $n_t$  is the density of trapped carriers at the onset voltage and  $e$  is the electronic charge. We describe the derivation of onset voltage in the Supporting Information. We note that  $n_t$  is only the total trap density in the semiconductor under certain explicit assumptions, which we discuss in the Supporting Information. With increasing voltage beyond  $V_{\text{ons}}$ , the current-

density increases sharply (3.  $J \propto V^n$  in Figure 1b). Once all traps are filled, the current is assumed to follow the Mott-Gurney law in the absence of trapping (4.  $J \propto V^2$  in Figure 1b).

Hybrid perovskites are distinct from most conventional semiconductors because they exhibit characteristics of both electronic and ionic conduction. The presence of these mobile ionic species has the potential to profoundly disturb device characteristics, because they may shield the bulk material from externally applied voltages and thus affect the total electronic current injection, transport and extraction. For instance, consensus has been reached that mobile ions play a major role in the origin of hysteresis in  $J$ - $V$  curves of solar cell devices.<sup>21–23</sup>

Despite the research effort toward exploring the origins of this ubiquitous hysteresis in  $J$ - $V$  curves for solar cells, there is a large body of published literature on SCLC measurements of metal halide perovskite single crystals and thin films that does not report data for both forward (increasing voltage) and reverse (decreasing voltage) directions in  $J$ - $V$  sweeps nor mentions the possible influences of mobile ions.<sup>24–46</sup> However, a redistribution of ionic charge due to a continuously applied electric field during the SCLC measurement is in fact likely to influence the electronic charge carrier transport in perovskites and thus the shape of the  $J$ - $V$  curve. Therefore, characterizing charge carrier properties without considering mobile ions is prone to misinterpretation and can lead to systematic errors that result in misunderstanding of the

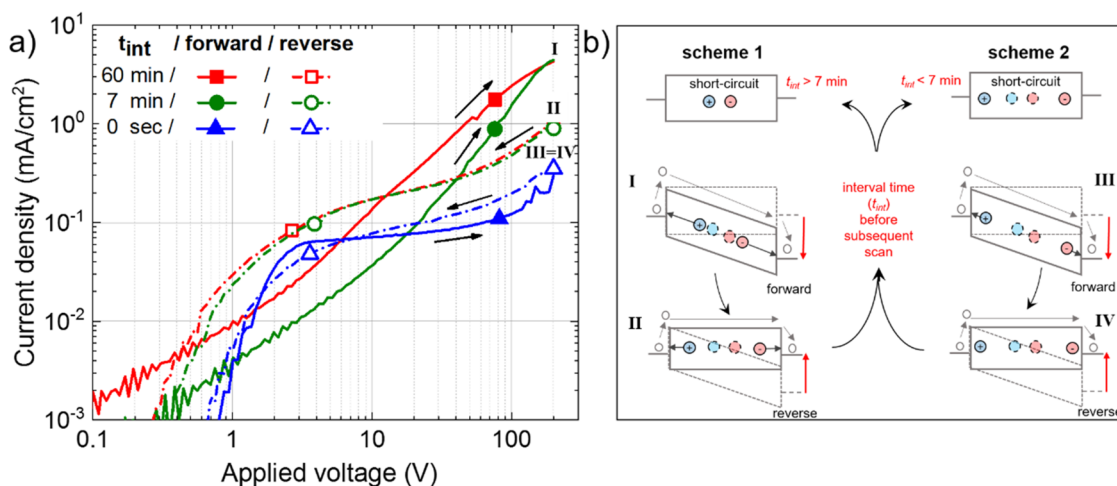


**Figure 2.** Time-dependent hysteresis in SCLC measurements and schematic illustration of mobile ions. (a) Large hysteresis between forward and reverse  $J$ - $V$  traces when  $t_{\text{int}} > t_{\text{ion-diff}}$  (red and green lines) and small hysteresis between forward and reverse  $J$ - $V$  traces when  $t_{\text{int}} < t_{\text{ion-diff}}$  (blue line). (b) Schematic illustration to explain the difference in hysteresis when  $t_{\text{int}} > t_{\text{ion-diff}}$  (scheme 1) and  $t_{\text{int}} < t_{\text{ion-diff}}$  (scheme 2). The arrows in situations I–IV in panel b give an indication of the respective distance traveled by ions in each situation. Situations I–IV in panel a are represented by the corresponding illustrations in panel b.

intrinsic electronic properties of perovskites. Because SCLC is such a popular and, in principle, simple measurement to perform, it is crucial to understand the effect of mobile ions under an applied electric field for an accurate characterization of the electrical properties.

Here, we show that  $V_{\text{ons}}$  in MAPbBr<sub>3</sub> single crystals can differ by more than an order of magnitude when the scan is swept between forward (0.1 to 200 V) and reverse (200 to 0.1 V) directions. We explain this hysteresis by analyzing the role of the applied electric field during the SCLC measurement on the mobile ions. To achieve reproducible  $J$ - $V$  curves without hysteresis, we introduce a pulsed voltage (PV)-SCLC method which pseudolocalizes nominally mobile ions during the  $J$ - $V$  sweep, enabling the measurement of the intrinsic electronic properties in perovskite semiconductors. Using the PV-SCLC method, we decouple ionic conductivity from electronic conductivity in macroscopic MAPbBr<sub>3</sub> single crystals during SCLC measurements, and calculate a lower bound of the trap density in MAPbBr<sub>3</sub> single crystals of  $2.8 \pm 1.8 \times 10^{12} \text{ cm}^{-3}$ .

**Hysteresis in Current–Voltage Curves during Space-Charge Limited Current Measurements.** For our study, we prepared free-standing, millimeter-sized macroscopic MAPbBr<sub>3</sub> single crystals with 120 nm thick gold electrodes on either side of the crystal for carrier injection and extraction (see Methods and Figure S1). We observe a significant difference between the  $J$ - $V$  scans performed in the forward (solid black line) and reverse (dashed black line) bias voltage directions during the SCLC measurement, as we show in Figure 1c. Surprisingly, to the best of our knowledge, this is the first time hysteresis in SCLC measurements of perovskites has been acknowledged. To understand this hysteretic behavior, we look into the principle of the SCLC measurement, as depicted in Figure 1d, with the assumption that we have mobile ionic species in the perovskite crystal. These species may originate from vacancies or interstitials. Under short-circuit conditions, we assume that mobile ions are distributed across the crystal (1. short circuit in Figure 1d). A positive voltage at the electron extraction contact during the forward voltage scan results in the drift of negatively charged mobile ions to the electron extraction electrode, while simultaneously positively charged mobile ions drift toward the

opposite electrode (2. forward scan in Figure 1d). While we change the scanning direction from high voltages back to short circuit, the internal electric field of the system is still under positive voltage conditions, and consequently mobile ions are still displaced toward the electrode interfaces (3. reverse scan in Figure 1d). This causes a “positive prebias effect” during the reverse voltage scan. We postulate that the difference in the position of mobile ions, caused by the applied electric field during the  $J$ - $V$  sweep, explains the hysteresis in the  $J$ - $V$  traces. Additionally, we assume that the mobile ions require a certain diffusion time under short-circuit conditions to migrate back to their initial position after drifting to electrode interfaces because of the applied electric field during the voltage sweep.

**Localizing Mobile Ions.** To assess the influence of drifting mobile ions on electronic current extraction, we control the localization of mobile ionic species as a function of time, by varying the waiting time (termed as interval time,  $t_{\text{int}}$ ) between subsequent voltage sweep cycles, where one voltage sweep cycle refers to both forward and reverse scan. The electrodes are left floating (at open-circuit) between voltage sweep cycles. During one voltage sweep cycle, we apply a continuously (stepwise and steady state without resting time between voltage steps) increasing electric field from 0.1 to 200 V and back from 200 to 0.1 V. A schematic of the scan routine is depicted in Figure S2. The change in hysteresis upon changing  $t_{\text{int}}$  is shown in Figure 2a. The red and blue lines show the extreme cases for  $t_{\text{int}}$  equal to 60 min and 0 s, respectively. Panels a and b of Figure S3 depict the stepwise change in the forward and reverse scans, respectively, when varying  $t_{\text{int}}$  from 60 min to 0 s in 24 steps, respectively. We observe “reproducible hysteresis” in the  $J$ - $V$  traces, when  $t_{\text{int}}$  is set to 7 min (green line).

We illustrate the effect of changing  $t_{\text{int}}$  in Figure 2b. We show in scheme 1 (Figure 2b) that the mobile ions have enough time to diffuse back to their initial position after the voltage sweep if the interval time between two subsequent voltage sweep cycles exceeds the average ionic diffusion time ( $t_{\text{ion-diff}}$ ), i.e.  $t_{\text{int}} > t_{\text{ion-diff}}$ . In this case, during the forward  $J$ - $V$  scan of the subsequent voltage sweep, the applied electric field causes a significant change in the position of ions, resulting in

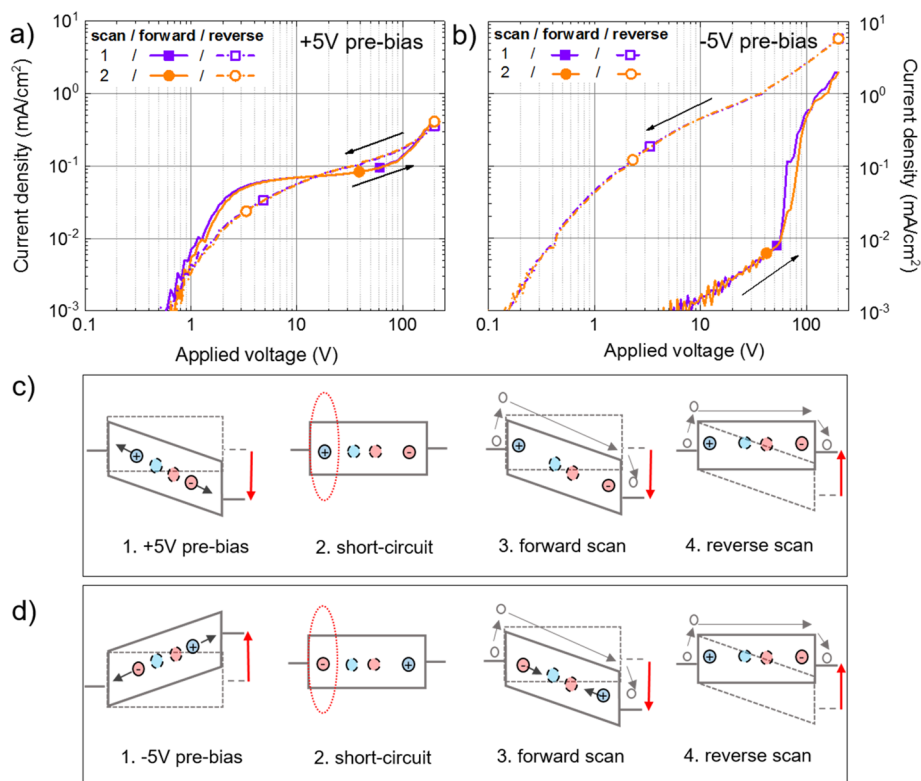


**Figure 3.** Prebias-dependent hysteresis in SCLC measurement and schematic illustration of mobile ions. (a) Small reproducible hysteresis in  $J$ - $V$  traces after applying +5 V prebias (solid and dashed lines for forward and reverse voltage sweep, respectively). (b) Large reproducible hysteresis in  $J$ - $V$  traces after applying -5 V prebias. (c) Schematic illustration of selective ion localization upon applying a positive prebias. A positive prebias causes ion migration toward the electrodes (1). After going back to short circuit, positive ions displaced toward the injection contact (2). Ions remain displaced toward the same electrodes during the forward scan (3) and reverse scan (4). (d) Schematic illustration of selective ion localization upon applying a negative prebias. A negative prebias results in ion migration toward the electrodes (1). After going back to short circuit, negative ions displaced toward the injection contact (2). Ions drift toward the opposite interface during the forward scan (3), as the polarity of the bias condition switches, and stay there during the reverse scan (4). Light blue and red dashed circles represent initial sites of positive and negative ions, respectively. Light blue and red solid circles represent positive and negative ions, respectively.

the reverse  $J$ - $V$  scan being significantly different from the forward-direction  $J$ - $V$  scan, manifesting as large hysteresis (red and green dashed lines in Figure 2a).

In scheme 2 (Figure 2b), we show that if the interval time before performing the next voltage sweep is smaller than the average ionic diffusion time ( $t_{\text{int}} < t_{\text{ion-diff}}$ ), there is insufficient time for the ions to diffuse back to their initial position before starting the next voltage scan, and the ionic distribution in the film remains predominantly perturbed. In this instance, where  $t_{\text{int}} < t_{\text{ion-diff}}$  both the forward and reverse scans (solid and dashed blue lines in Figure 2a) are very similar and more closely resemble the reverse sweep of the initial scan. This is consistent with the positions of the ions being approximately fixed during the scan but perturbed in comparison with the “unbiased” crystal.

Additionally, we note a large current gap at 200 V at the point where we switch voltage scan direction from forward to reverse when  $t_{\text{int}} > t_{\text{ion-diff}}$  (denoted by points I and II in Figure 2a), whereas we do not observe this current gap at 200 V when  $t_{\text{int}} < t_{\text{ion-diff}}$  (denoted by points III and IV in Figure 2a). We attribute this current gap to the fact that there is a finite time (40 ms) taken for the system to start the reverse scan (at 200 V), and a strong forward biasing effect is occurring during this dwell time.

At large forward biases (200 V) the initial current density in the forward direction scan is more than 1 order of magnitude greater than the current density at the same voltage after forward biasing. The forward prebias effect clearly suppresses the current flowing through the crystal. We expect the mobile ions to diffuse from the bulk of the perovskite toward the electrodes, when under bias. The suppression of current density may therefore be explained by either the screening of the externally applied electric field to regions near the contacts or a change to the bulk mobility of the perovskite, which may be due to the generation or activation of traps within the perovskite, or a combination of the two.

To further understand the role of the prebias effect upon hysteresis, we apply the prebias (+5 or -5 V) for 120 s to the electrodes before performing the  $J$ - $V$  scans. Figure 3a shows reproducible  $J$ - $V$  curves with little hysteresis upon applying a positive prebias of 5 V, whereas Figure 3b shows reproducible  $J$ - $V$  traces with large hysteresis when the polarity of the prebias is switched to -5 V. We schematically illustrate how we expect mobile ions to behave upon applying a positive and negative prebias in panels c and d of Figure 3, respectively. Figure 3c represents how positive mobile ions drift toward the carrier injection contact, while negative mobile ions drift toward the opposite electrode, upon applying a positive voltage (1). When the system is back at short circuit, the positive

mobile ions are displaced toward the injection contact, while negative mobile ions are displaced toward the other contact (2). When the  $J$ - $V$  sweep is performed directly after prebiasing, the mobile ions have no time to diffuse away from the interfaces. Thus, positive and negative ions are displaced toward the electrode interfaces, during both forward (3) and reverse (4) scans. This is in agreement with the small hysteresis in Figure 3a, because both forward and reverse voltage scan directions are performed under positive prebias conditions. The similarities between Figure 3a and the blue line in Figure 2a support the concept of the positive prebias effect as a result of both positive and negative ions separately displacing toward the electrodes.

The schematics in Figure 3d describe how the mechanism is reversed when we switch the polarity of the prebias from positive to negative voltage. Upon application of the negative prebias, negative mobile ions drift toward the electron injection contact, while positive mobile ions drift toward the other contact (1). After going back to short circuit, the respective mobile ions are displaced toward the electrode interfaces (2). During the subsequent forward scan, the bias conditions switch in polarity and mobile ions drift across the crystal toward the opposite electrode (3) with the ionic current, moving in the same direction as the electronic current. During the following reverse  $J$ - $V$  scan, the mobile ions are again displaced toward the opposite electrode interfaces (4), generating the positive prebias effect during the reverse scan. The switch from a negative to a positive prebias effect during the voltage sweep corroborates with the observed large hysteresis, as we show in Figure 3b. In Figure S5, we depict the reproducibility of the  $J$ - $V$  traces when we displace the ions toward the electrode interfaces. We note that all continuous stepwise voltage measurements have been performed on the same device in the dark under vacuum ( $10^{-4}$  mbar) at room temperature.

Although we have identified the origin of the positive (negative) prebias effect, and therefore the root of hysteresis, the net displacement of ionic charge and a perturbation of the electric field through the crystal will still effect the charge carrier injection and electronic conductivity. This makes it difficult to determine physical properties from the measurement. It would therefore be advantageous to devise a measurement protocol which circumvents the influence of mobile ions.

**Pulsed Voltage Space-Charge Limited Current Measurements.** We introduce a well-defined transient pulsed voltage in the SCLC measurement, with an extreme difference between measurement time and rest time, to obtain accurate current-voltage curves from SCLC measurements without redistributing mobile ions through the single crystal while measuring. From transient current measurements (shown in Figure S4) we found that we can hold a fixed voltage across the crystal for more than 100 ms, before the current flow through the device begins to be perturbed, presumably by ionic redistribution. To further ensure this, we measure the current as a function of time for both 20 and 200 ms integration time, as we show in Figure S6. We observe that a 20 ms integration time for voltage pulses is short enough for accurate electronic current measurements during the PV-SCLC measurement. We therefore apply this voltage pulse width of 20 ms, and we set the time between voltage pulses ( $t_{bvp}$ ) to 7 min, which we had previously determined to be the average ionic redistribution time after one voltage sweep. We go back to short circuit

during  $t_{bvp}$  to let the mobile ions diffuse back to their initial position after every voltage pulse to eliminate the prebias effect. We show a schematic of the pulsed voltage measurement in Figure 4a (1) and the respective ion position in Figure 4a (2).

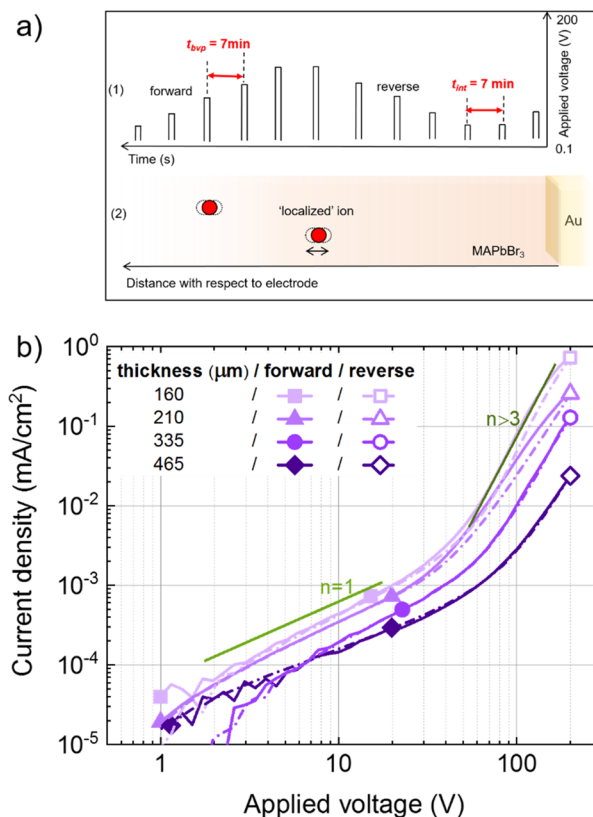


**Figure 4.** Thickness-dependent PV-SCLC measurement. (a) Schematic illustration of the PV-SCLC measurement (1) and the respective “localized” ion motion (2). Both  $t_{bvp}$  and  $t_{int}$  are set to 7 min during the PV-SCLC measurement. (b) Thickness-dependent  $J$ - $V$  traces without hysteresis extracted from the PV-SCLC measurement.

In Figure 4b, we show the resulting  $J$ - $V$  curves from MAPbBr<sub>3</sub> single crystals with different thicknesses. When we set  $t_{bvp} > t_{ion-diff}$  during the SCLC measurement, as is the case for  $t_{bvp} = 7$  min, we obtain reproducible, nonhysteretic  $J$ - $V$  characteristics from all single crystals. The lack of hysteresis is consistent with the ions remaining localized in their original positions, or close enough so as not to significantly perturb the  $J$ - $V$  characteristics, during the short voltage pulses of the measurement. Because we are limited by the voltage range of our instrument, not all possible regimes of a typical SCLC measurement are observable for all thicknesses; in particular, we are not able to access the Mott-Gurney regime which is equivalent to trap-free SCLC (corresponding to all traps in the material being filled). Nevertheless, the current range studied reveals a rich variety of characteristics. All thicknesses show a clear Ohmic region ( $J \propto V^{n=1}$ ) at low voltages, from which the conductivity ( $\sigma$ ) can be determined following  $\sigma = \frac{L}{AR}$ , where  $L$  is the thickness of the crystal,  $A$  the area, and  $R$  the resistance. The conductivity is calculated to be  $6.9 \pm 0.3 \times 10^{-10} \text{ S cm}^{-1}$ . We note that this is about 1 order of magnitude lower than previously reported conductivity values extracted

from SCLC measurements on single crystals.<sup>24,27,33</sup> This is in agreement with our results that the electron current is influenced by the ionic conduction, as previously explained and shown in Figures 2, S4, and S6. After the Ohmic regime, we observe a gradual increase in gradient in the  $J$ - $V$  characteristics and a transition into the  $n \geq 3$  region, because of the filling of trap states with increasing electric field. We extract  $V_{\text{ons}}$  for 160, 210, 335, and 465  $\mu\text{m}$  thick crystals to be 48, 49, 70, and 91 V, respectively.

To assess whether eq 2 can be used to estimate trap densities from  $V_{\text{ons}}$ , we perform numerical simulations to gauge the influence of ionic species on SCLC measurements. We use a one-dimensional drift-diffusion model that includes electrons and holes as well as ionic species (see the Supporting Information for details).<sup>47-49</sup> The simulation mimics the pulsed voltage measurements by first calculating the ionic distribution at zero voltage and then sweeping the voltage while keeping the ions fixed. This procedure recreates current-voltage measurements without redistributing mobile ions throughout the crystal. We find that, in the absence of ions, the simulated  $I$ - $V$  characteristics indeed show a voltage regime that corresponds to the filling of traps, as shown by the dashed line in Figure 5. However, mobile ions also contribute

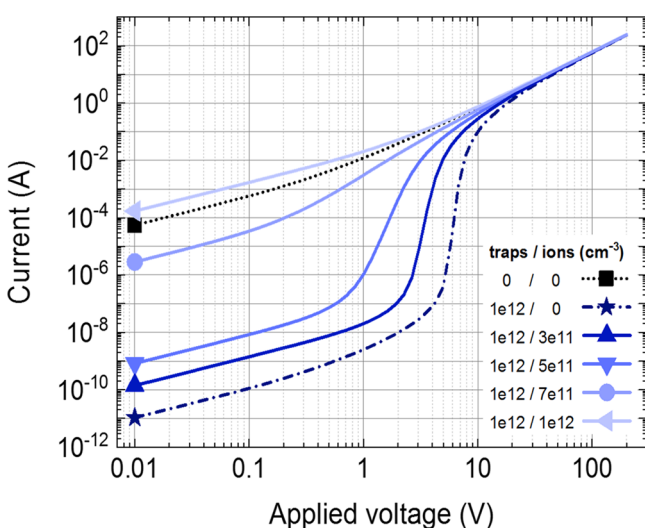


**Figure 5.** Simulated current-voltage characteristics during pulsed voltage SCLC measurements. Modeled  $I$ - $V$  curve for a 170  $\mu\text{m}$  electron-only device with trap states and mobile ions.  $V_{\text{ons}}$  shifts to lower voltages when an ion density which is lower than, but within an order of magnitude of the trap density, is added to the system. If the ion density is equal to, or greater than, the trap density, the effect of traps is strongly overshadowed by the ions.

space-charge in the bulk of the crystal, effectively negating the charge of trapped electrons. As more ions are introduced, the  $V_{\text{ons}}$  shift to lower voltages, and eventually the effect of traps disappears (see Figure 5). Equation 2, therefore, yields only a lower limit of the trap density.

While eq 2 underestimates the number of traps if there are mobile ions, the simulations also show that traps dominate (i.e., outnumber mobile ions) if the onset voltage ( $V_{\text{ons}}$ ) can be observed. Moreover, the simulated  $I$ - $V$  curves also reveal that  $V_{\text{ons}}$  reduces by only up to 1 order of magnitude before it is undeterminable. In other words, eq 2 underestimates the density of the trapped carriers because of the presence of ions by no more than 1 order of magnitude.

We emphasize that in order to quantify the actual trap density, the distribution of traps should be known.<sup>15</sup> Conventionally, the trap-filling regime is modeled on a single trap level, where we would expect to observe a rapid increase in current density within increasing applied bias, as we pass the trap-filling onset voltage, whereas a broader trap distribution results in a more gradual rise in current after  $V_{\text{ons}}$ . Because we observe a gradual rise in current after  $V_{\text{ons}}$ , we can only attribute a lower bound to the trap density from the  $V_{\text{ons}}$  and we are specifically determining the density of trapped carriers at this specific voltage point, rather than the total density of traps. In our case here this is equal to  $2.8 \pm 1.8 \times 10^{12} \text{ cm}^{-3}$ . After all the trap states are filled, we should be able to measure the bulk properties in the single crystals, as we enter the space-charge limited regime in the absence of traps, where  $J \propto V^{m=2}$ . However, even for the thinnest crystals we have studied here, we do not conclusively enter this regime within the voltage range of our measurement. Hence, we have not determined the SCLC charge carrier mobility for the samples we have studied here.

We have shown how mobile ions can have a dramatic effect on electronic current extraction during SCLC measurements, masking the underlying fundamental electronic properties of the semiconductor. To circumvent this, we have introduced a pulsed voltage space-charge limited current measurement methodology, which diminishes the motion of mobile ions. This allows us to obtain  $J$ - $V$  curves without hysteresis from semiconductors that exhibit both ionic and electronic conductivity. Our results from this revised voltage scanning protocol finally resolve the ambiguities that surround similar electronic measurements of metal halide perovskite single crystals. We have established a method to accurately measure the electronic properties and trap characteristics, without perturbation in the electronic current flow by the motion of mobile ions. From the resulting  $J$ - $V$  traces, we determine a lower bound of the trap density in MAPbBr<sub>3</sub> single crystals to be  $2.8 \pm 1.8 \times 10^{12} \text{ cm}^{-3}$ . With this work, we highlight that in order to accurately interpret perovskite-based device measurements and achieve comparability between different laboratories, the experimental conditions and analysis routines should be clearly described and carefully conducted because of the combined ionic and electronic nature of perovskites. More accurate measurements of the fundamental properties of these materials should ultimately lead to more effective development of their optoelectronic devices.

## METHODS

**Chemicals and Reagents.** *N,N*-Dimethylformamide (DMF) (68-12-2), PbBr<sub>2</sub> (10031-22-8), and CH<sub>3</sub>NH<sub>3</sub>Br (6876-37-5) were purchased from Sigma-Aldrich. All salts and solvents were used as received and without any further purification.

**Synthesis of MAPbBr<sub>3</sub> Single Crystals and Device Fabrication.** MAPbBr<sub>3</sub> single crystals were fabricated from a seed MAPbBr<sub>3</sub> crystal by following a previously published experimental protocol.<sup>50,51</sup> PbBr<sub>2</sub> (3.67 g) and CH<sub>3</sub>NH<sub>3</sub>Br (1.11 g) were dissolved in 10 mL of DMF. The solution was stirred until fully transparent. This solution was filtered with a 25 mm diameter 0.45  $\mu\text{m}$  PVDF filter. A 4 mL sample of the filtrate was placed in a vial which contained a seed MAPbBr<sub>3</sub> crystal. To control the thickness down to the micrometer scale, a small chamber was constructed using two thin glass plates of different thicknesses placed on the bottom of the glass vial with a gap in between and a cover glass on top. The vial was kept in an oil

bath undisturbed at 80 °C for 5 h. A free-standing, millimeter-sized crystal was taken out of the vial once formed and quickly rinsed by pure DMF solvent. A schematic of the single-crystal growth and device fabrication process is depicted in Figure S1.

**Measurement and Characterization.** The 120 nm gold electrodes were evaporated on both of the larger faces of the single crystal by an evaporator (Kurt J. Lesker, Nano36) at a 0.5 A s<sup>-1</sup> deposition rate. The *J*–*V* traces were measured using a computer-controlled<sup>52</sup> 2400 Series Keithley source meter in the dark under vacuum at room temperature. The vacuum pump (Leybold vacuum, PT 70 F-Compact) pumped the system down to 10<sup>-4</sup> mbar.

## ■ ASSOCIATED CONTENT

### Supporting Information

The Supporting Information is available free of charge at <https://pubs.acs.org/doi/10.1021/acsnenergylett.9b02720>.

Derivation of the onset voltage; schematic illustration of the device fabrication process (Figure S1); schematic illustration of the continuous (stepwise and steady-state) applied voltage during full voltage sweep (Figure S2); time-dependent hysteresis in SCLC measurements (Figure S3); transient current measurement (Figure S4); prebias-dependent hysteresis in SCLC measurements (Figure S5); transient current measurement (Figure S6); parameters used in the device simulation to investigate the correlation of mobile ions and traps (Table S1); simulation details; references (PDF)

## ■ AUTHOR INFORMATION

### Corresponding Authors

**L. Jan Anton Koster** – University of Groningen, Groningen, The Netherlands; [orcid.org/0000-0002-6558-5295](https://orcid.org/0000-0002-6558-5295); Email: [l.j.a.koster@rug.nl](mailto:l.j.a.koster@rug.nl)

**Henry J. Snaith** – University of Oxford, Oxford, United Kingdom; [orcid.org/0000-0001-8511-790X](https://orcid.org/0000-0001-8511-790X); Email: [henry.snaith@physics.ox.ac.uk](mailto:henry.snaith@physics.ox.ac.uk)

**Jongchul Lim** – University of Oxford, Oxford, United Kingdom; [orcid.org/0000-0001-8609-8747](https://orcid.org/0000-0001-8609-8747); Email: [jongchul.lim@physics.ox.ac.uk](mailto:jongchul.lim@physics.ox.ac.uk)

### Other Authors

**Elisabeth A. Duijnste** – University of Oxford, Oxford, United Kingdom; [orcid.org/0000-0002-7002-1523](https://orcid.org/0000-0002-7002-1523)

**James M. Ball** – University of Oxford, Oxford, United Kingdom; [orcid.org/0000-0003-1730-5217](https://orcid.org/0000-0003-1730-5217)

**Vincent M. Le Corre** – University of Groningen, Groningen, The Netherlands; [orcid.org/0000-0001-6365-179X](https://orcid.org/0000-0001-6365-179X)

Complete contact information is available at: <https://pubs.acs.org/10.1021/acsnenergylett.9b02720>

### Author Contributions

E.A.D. and J.L. fabricated the devices, performed experiments, and analyzed data. J.M.B. wrote the control software and assisted with the experimental setup and measurements. E.A.D., V.M.L.C., and L.J.A.K. performed numerical simulations. E.A.D., J.L., and H.J.S. wrote the manuscript. All authors discussed the results and reviewed the manuscript. J.L., H.J.S., and L.J.A.K. guided and supervised the overall project.

## Notes

The authors declare the following competing financial interest(s): H.J.S. is cofounder and CSO of Oxford PV Ltd, a company commercializing perovskite PV technology.

## ■ ACKNOWLEDGMENTS

This project was funded by the Engineering and Physical Sciences Research Council (EPSRC), Grants EP/M005143/1 and EP/P006329/1. E.A.D. thanks the EPSRC for funding via the Centre for Doctoral Training in New and Sustainable Photovoltaics. The work by V.L.C. is supported by a grant from STW/NWO (VIDI 13476). This is a publication by the FOM Focus Group “Next Generation Organic Photovoltaics”, participating in the Dutch Institute for Fundamental Energy Research (DIFFER).

## ■ REFERENCES

- (1) Kojima, A.; Teshima, K.; Shirai, Y.; Miyasaka, T. Organometal Halide Perovskites as Visible-Light Sensitizers for Photovoltaic Cells. *J. Am. Chem. Soc.* **2009**, *131* (17), 6050–6051.
- (2) Lee, M. M.; Teuscher, J.; Miyasaka, T.; Murakami, T. N.; Snaith, H. J. Efficient Hybrid Solar Cells Based on Meso-Superstructured Organometal Halide Perovskites. *Science* **2012**, *338* (6107), 643–647.
- (3) Chang, J. A.; Im, S. H.; Lee, Y. H.; Kim, H. J.; Lim, C. S.; Heo, J. H.; Seok, S. I. Panchromatic Photon-Harvesting by Hole-Conducting Materials in Inorganic-Organic Heterojunction Sensitized-Solar Cell through the Formation of Nanostructured Electron Channels. *Nano Lett.* **2012**, *12* (4), 1863–1867.
- (4) Lim, J.; Hörantner, M. T.; Sakai, N.; Ball, J. M.; Mahesh, S.; Noel, N. K.; Lin, Y. H.; Patel, J. B.; McMeekin, D. P.; Johnston, M. B.; et al. Elucidating the Long-Range Charge Carrier Mobility in Metal Halide Perovskite Thin Films. *Energy Environ. Sci.* **2019**, *12* (1), 169–176.
- (5) NREL. Efficiency Chart. <https://www.nrel.gov/pv/cell-efficiency.html> (accessed Aug 12, 2019).
- (6) Chin, X. Y.; Cortecchia, D.; Yin, J.; Bruno, A.; Soci, C. Lead Iodide Perovskite Light-Emitting Field-Effect Transistor. *Nat. Commun.* **2015**, *6* (1), 7383.
- (7) Tan, Z. K.; Moghaddam, R. S.; Lai, M. L.; Docampo, P.; Higler, R.; Deschler, F.; Price, M.; Sadhanala, A.; Pazos, L. M.; Credgington, D.; et al. Bright Light-Emitting Diodes Based on Organometal Halide Perovskite. *Nat. Nanotechnol.* **2014**, *9* (9), 687–692.
- (8) Dong, R.; Fang, Y.; Chae, J.; Dai, J.; Xiao, Z.; Dong, Q.; Yuan, Y.; Centrone, A.; Zeng, X. C.; Huang, J. High-Gain and Low-Driving-Voltage Photodetectors Based on Organolead Triiodide Perovskites. *Adv. Mater.* **2015**, *27* (11), 1912–1918.
- (9) Zhu, H.; Fu, Y.; Meng, F.; Wu, X.; Gong, Z.; Ding, Q.; Gustafsson, M. V.; Trinh, M. T.; Jin, S.; Zhu, X. Y. Lead Halide Perovskite Nanowire Lasers with Low Lasing Thresholds and High Quality Factors. *Nat. Mater.* **2015**, *14* (6), 636–642.
- (10) Xing, G.; Mathews, N.; Lim, S. S.; Yantara, N.; Liu, X.; Sabba, D.; Grätzel, M.; Mhaisalkar, S.; Sum, T. C. Low-Temperature Solution-Processed Wavelength-Tunable Perovskites for Lasing. *Nat. Mater.* **2014**, *13* (5), 476–480.
- (11) Peng, J.; Chen, Y.; Zheng, K.; Pullerits, T.; Liang, Z. Insights into Charge Carrier Dynamics in Organo-Metal Halide Perovskites: From Neat Films to Solar Cells. *Chem. Soc. Rev.* **2017**, *46* (19), 5714–5729.
- (12) Robertson, J. H. Electrical Transport in Solids, with Particular Reference to Organic Semiconductors by K. C. Kao and W. Hwang. *Acta Crystallogr., Sect. B: Struct. Crystallogr. Cryst. Chem.* **1982**, *38* (1), 350–350.
- (13) Sze, S. M.; Ng, K. K. *Physics of Semiconductor Devices*, 3rd ed.; 2006.
- (14) Sze, S. M.; Lee, M. K. *Semiconductor Devices: Physics and Technology*; Wiley, 2012.

- (15) Stoneham, A. M. *Current Injection in Solids*; Academic Press, 1970; Vol. 21.
- (16) Röhr, J. A.; Kirchartz, T.; Nelson, J. On the Correct Interpretation of the Low Voltage Regime in Intrinsic Single-Carrier Devices. *J. Phys.: Condens. Matter* **2017**, *29* (20), 205901.
- (17) D, J. V. Electronic Processes in Ionic Crystals (Mott, N. F.; Gurney, R. W.). *J. Chem. Educ.* **1965**, *42* (9), A692.
- (18) Poglitsch, A.; Weber, D. Dynamic Disorder in Methylammoniumtrihalogenoplumbates (II) Observed by Millimeter-Wave Spectroscopy. *J. Chem. Phys.* **1987**, *87* (11), 6373–6378.
- (19) Lampert, M. A. Simplified Theory of Space-Charge-Limited Currents in an Insulator with Traps. *Phys. Rev.* **1956**, *103* (6), 1648–1656.
- (20) Van Woudenberg, T.; Blom, P. W. M.; Huiberts, J. N. Electro-Optical Properties of a Polymer Light-Emitting Diode with an Injection-Limited Hole Contact. *Appl. Phys. Lett.* **2003**, *82* (6), 985–987.
- (21) Snaith, H. J.; Abate, A.; Ball, J. M.; Eperon, G. E.; Leijtens, T.; Noel, N. K.; Stranks, S. D.; Wang, J. T. W.; Wojciechowski, K.; Zhang, W. Anomalous Hysteresis in Perovskite Solar Cells. *J. Phys. Chem. Lett.* **2014**, *5* (9), 1511–1515.
- (22) Moia, D.; Gelmetti, I.; Calado, P.; Fisher, W.; Stringer, M.; Game, O.; Hu, Y.; Docampo, P.; Lidzey, D.; Palomares, E.; et al. Ionic-to-Electronic Current Amplification in Hybrid Perovskite Solar Cells: Ionically Gated Transistor-Interface Circuit Model Explains Hysteresis and Impedance of Mixed Conducting Devices. *Energy Environ. Sci.* **2019**, *12* (4), 1296–1308.
- (23) Tress, W. Metal Halide Perovskites as Mixed Electronic-Ionic Conductors: Challenges and Opportunities - From Hysteresis to Memristivity. *J. Phys. Chem. Lett.* **2017**, *8* (13), 3106–3114.
- (24) Zhumekenov, A. A.; Saidaminov, M. I.; Haque, M. A.; Alarousu, E.; Sarmah, S. P.; Murali, B.; Dursun, I.; Miao, X. H.; Abdelhady, A. L.; Wu, T.; et al. Formamidinium Lead Halide Perovskite Crystals with Unprecedented Long Carrier Dynamics and Diffusion Length. *ACS Energy Lett.* **2016**, *1* (1), 32–37.
- (25) Lian, Z.; Yan, Q.; Gao, T.; Ding, J.; Lv, Q.; Ning, C.; Li, Q.; Sun, J. L. Perovskite CH<sub>3</sub>NH<sub>3</sub>PbI<sub>3</sub> (Cl) Single Crystals: Rapid Solution Growth, Unparalleled Crystalline Quality, and Low Trap Density toward 10<sup>8</sup> cm<sup>-3</sup>. *J. Am. Chem. Soc.* **2016**, *138* (30), 9409–9412.
- (26) Gu, Z.; Huang, Z.; Li, C.; Li, M.; Song, Y. A General Printing Approach for Scalable Growth of Perovskite Single-Crystal Films. *Sci. Adv.* **2018**, *4* (6), No. eaat2390.
- (27) Stranks, S. D.; Eperon, G. E.; Grancini, G.; Menelaou, C.; Alcocer, M. J. P.; Leijtens, T.; Herz, L. M.; Petrozza, A.; Snaith, H. J. Electron-Hole Diffusion Lengths Exceeding 1 Micrometer in an Organometal Trihalide Perovskite Absorber. *Science* **2013**, *342* (6156), 341–344.
- (28) Saidaminov, M. I.; Abdelhady, A. L.; Murali, B.; Alarousu, E.; Burlakov, V. M.; Peng, W.; Dursun, I.; Wang, L.; He, Y.; MacUlan, G.; et al. High-Quality Bulk Hybrid Perovskite Single Crystals within Minutes by Inverse Temperature Crystallization. *Nat. Commun.* **2015**, *6* (1), 7586.
- (29) Peng, W.; Wang, L.; Murali, B.; Ho, K. T.; Bera, A.; Cho, N.; Kang, C. F.; Burlakov, V. M.; Pan, J.; Sinatra, L.; et al. Solution-Grown Monocrystalline Hybrid Perovskite Films for Hole-Transporter-Free Solar Cells. *Adv. Mater.* **2016**, *28* (17), 3383–3390.
- (30) Adinolfi, V.; Yuan, M.; Comin, R.; Thibau, E. S.; Shi, D.; Saidaminov, M. I.; Kanjanaboos, P.; Kopilovic, D.; Hoogland, S.; Lu, Z. H.; et al. The In-Gap Electronic State Spectrum of Methylammonium Lead Iodide Single-Crystal Perovskites. *Adv. Mater.* **2016**, *28* (17), 3406–3410.
- (31) Saidaminov, M. I.; Adinolfi, V.; Comin, R.; Abdelhady, A. L.; Peng, W.; Dursun, I.; Yuan, M.; Hoogland, S.; Sargent, E. H.; Bakr, O. M. Planar-Integrated Single-Crystalline Perovskite Photodetectors. *Nat. Commun.* **2015**, *6* (1), 8724.
- (32) Liu, Y.; Zhang, Y.; Yang, Z.; Yang, D.; Ren, X.; Pang, L.; Liu, S. F. Perovskite Wafers: Thinness- and Shape-Controlled Growth for Ultrathin Single-Crystalline Perovskite Wafers for Mass Production of Superior Photoelectronic Devices. *Adv. Mater.* **2016**, *28* (41), 9203–9203.
- (33) Shi, D.; Adinolfi, V.; Comin, R.; Yuan, M.; Alarousu, E.; Buin, A.; Chen, Y.; Hoogland, S.; Rothenberger, A.; Katsiev, K.; et al. Low Trap-State Density and Long Carrier Diffusion in Organolead Trihalide Perovskite Single Crystals. *Science* **2015**, *347* (6221), 519–522.
- (34) Lin, K.; Xing, J.; Quan, L. N.; de Arquer, F. P. G.; Gong, X.; Lu, J.; Xie, L.; Zhao, W.; Zhang, D.; Yan, C.; et al. Perovskite Light-Emitting Diodes with External Quantum Efficiency Exceeding 20%. *Nature* **2018**, *562* (7726), 245–248.
- (35) Chen, Y. X.; Ge, Q. Q.; Shi, Y.; Liu, J.; Xue, D. J.; Ma, J. Y.; Ding, J.; Yan, H. J.; Hu, J. S.; Wan, L. J. General Space-Confined On-Substrate Fabrication of Thickness-Adjustable Hybrid Perovskite Single-Crystalline Thin Films. *J. Am. Chem. Soc.* **2016**, *138* (50), 16196–16199.
- (36) Liu, Y.; Yang, Z.; Cui, D.; Ren, X.; Sun, J.; Liu, X.; Zhang, J.; Wei, Q.; Fan, H.; Yu, F.; et al. Two-Inch-Sized Perovskite CH<sub>3</sub>NH<sub>3</sub>PbX<sub>3</sub> (X = Cl, Br, I) Crystals: Growth and Characterization. *Adv. Mater.* **2015**, *27* (35), 5176–5183.
- (37) Wei, H.; Desantis, D.; Wei, W.; Deng, Y.; Guo, D.; Savenije, T. J.; Cao, L.; Huang, J. Dopant Compensation in Alloyed CH<sub>3</sub>NH<sub>3</sub>PbBr<sub>3-x</sub>Cl<sub>x</sub> Perovskite Single Crystals for Gamma-Ray Spectroscopy. *Nat. Mater.* **2017**, *16* (8), 826–833.
- (38) Rao, H. S.; Li, W. G.; Chen, B. X.; Kuang, D. B.; Su, C. Y. In Situ Growth of 120 cm<sup>2</sup> CH<sub>3</sub>NH<sub>3</sub>PbBr<sub>3</sub> Perovskite Crystal Film on FTO Glass for Narrowband-Photodetectors. *Adv. Mater.* **2017**, *29* (16), 1602639.
- (39) Huang, Y.; Li, L.; Liu, Z.; Jiao, H.; He, Y.; Wang, X.; Zhu, R.; Wang, D.; Sun, J.; Chen, Q.; et al. The Intrinsic Properties of FA<sub>(1-x)</sub>MA<sub>x</sub>PbI<sub>3</sub> Perovskite Single Crystals. *J. Mater. Chem. A* **2017**, *5* (18), 8537–8544.
- (40) Liu, Y.; Sun, J.; Yang, Z.; Yang, D.; Ren, X.; Xu, H.; Yang, Z.; Liu, S. F. 20-mm-Large Single-Crystalline Formamidinium-Perovskite Wafer for Mass Production of Integrated Photodetectors. *Adv. Opt. Mater.* **2016**, *4* (11), 1829–1837.
- (41) Murali, B.; Yengel, E.; Yang, C.; Peng, W.; Alarousu, E.; Bakr, O. M.; Mohammed, O. F. The Surface of Hybrid Perovskite Crystals: A Boon or Bane. *ACS Energy Lett.* **2017**, *2* (4), 846–856.
- (42) Han, Q.; Bae, S. H.; Sun, P.; Hsieh, Y. T.; Yang, Y.; Rim, Y. S.; Zhao, H.; Chen, Q.; Shi, W.; Li, G.; et al. Single Crystal Formamidinium Lead Iodide (FAPbI<sub>3</sub>): Insight into the Structural, Optical, and Electrical Properties. *Adv. Mater.* **2016**, *28* (11), 2253–2258.
- (43) Zheng, G.; Zhu, C.; Ma, J.; Zhang, X.; Tang, G.; Li, R.; Chen, Y.; Li, L.; Hu, J.; Hong, J.; et al. Manipulation of Facet Orientation in Hybrid Perovskite Polycrystalline Films by Cation Cascade. *Nat. Commun.* **2018**, *9* (1), 2793.
- (44) Chen, Z.; Dong, Q.; Liu, Y.; Bao, C.; Fang, Y.; Lin, Y.; Tang, S.; Wang, Q.; Xiao, X.; Bai, Y.; et al. Thin Single Crystal Perovskite Solar Cells to Harvest Below-Bandgap Light Absorption. *Nat. Commun.* **2017**, *8* (1), 1890.
- (45) Liu, Y.; Zhang, Y.; Yang, Z.; Ye, H.; Feng, J.; Xu, Z.; Zhang, X.; Munir, R.; Liu, J.; Zuo, P.; et al. Multi-Inch Single-Crystalline Perovskite Membrane for High-Detectivity Flexible Photosensors. *Nat. Commun.* **2018**, *9* (1), 5302.
- (46) Ju, D.; Dang, Y.; Zhu, Z.; Liu, H.; Chueh, C. C.; Li, X.; Wang, L.; Hu, X.; Jen, A. K. Y.; Tao, X. Tunable Band Gap and Long Carrier Recombination Lifetime of Stable Mixed CH<sub>3</sub>NH<sub>3</sub>Pb<sub>x</sub>Sn<sub>1-x</sub>Br<sub>3</sub> Single Crystals. *Chem. Mater.* **2018**, *30* (5), 1556–1565.
- (47) Sherkar, T. S.; Momblona, C.; Gil-Escrig, L.; Bolink, H. J.; Koster, L. J. A. Improving Perovskite Solar Cells: Insights From a Validated Device Model. *Adv. Energy Mater.* **2017**, *7* (13), 1602432.
- (48) Sherkar, T. S.; Momblona, C.; Gil-Escrig, L.; Ávila, J.; Sessolo, M.; Bolink, H. J.; Koster, L. J. A. Recombination in Perovskite Solar Cells: Significance of Grain Boundaries, Interface Traps, and Defect Ions. *ACS Energy Lett.* **2017**, *2* (5), 1214–1222.
- (49) Le Corre, V. M.; Stolterfoht, M.; Perdigón Toro, L.; Feuerstein, M.; Wolff, C.; Gil-Escrig, L.; Bolink, H. J.; Neher, D.; Koster, L. J. A.

Charge Transport Layers Limiting the Efficiency of Perovskite Solar Cells: How to Optimize Conductivity, Doping, and Thickness. *ACS Appl. Energy Mater.* **2019**, *2* (9), 6280–6287.

(50) Nayak, P. K.; Moore, D. T.; Wenger, B.; Nayak, S.; Haghighirad, A. A.; Fineberg, A.; Noel, N. K.; Reid, O. G.; Rumbles, G.; Kukura, P.; et al. Mechanism for Rapid Growth of Organic-Inorganic Halide Perovskite Crystals. *Nat. Commun.* **2016**, *7* (1), 13303.

(51) Wenger, B.; Nayak, P. K.; Wen, X.; Kesava, S. V.; Noel, N. K.; Snaith, H. J. Consolidation of the Optoelectronic Properties of  $\text{CH}_3\text{NH}_3\text{PbBr}_3$  Perovskite Single Crystals. *Nat. Commun.* **2017**, *8* (1), 590.

(52) Ball, J. M. *jmball/SCLC*, first release (version v1.0.0); 2019; DOI: [10.5281/Zenodo.3369666](https://doi.org/10.5281/Zenodo.3369666).